

Figure 1. Instrumental set-up. (a) Summary of the on-chip multi-imaging flow cytometry system. The system was composed of seven major modules: (i) microchip, (ii) bright-field (BF) imaging, (iii) fluorescent (FL) detection, (iv) multi-view, (v) CCD camera, (vi) sorting, and (vii) controller, as numbered in the figure. (b) Summary of the multi-view module. (c) A photograph of the system.
doi:10.1371/journal.pone.0104372.g001

Results

Development of on-chip multi-imaging flow cytometry system

The on-chip multi-imaging flow cytometry system (Fig. 1) was composed of seven major modules as an improvement of previous systems [11–13,26]: (i) microchip, (ii) bright-field (BF) light source, (iii) fluorescent (FL) excitation and detection, (iv) multi-view, (v) CCD camera, (vi) sorting, and (vii) controller, as numbered in Fig. 1 (a). In the BF light source module, an LED (625 nm wavelength) was used as a source for taking BF images and was irradiated from the top of the chip. This allowed simultaneous measurements of both BF and FL images, avoiding interference of the wavelengths during the measurements. An objective lens having 20 \times magnification and a 0.75 numerical aperture was set to the system, which allowed clear cell images to be taken within the depth range of the microchannel (25 μ m) [27]. The FL excitation and detection modules contained three excitation lasers (375, 488, and 515 nm) and photomultipliers (PMTs), respectively, to monitor three different FL signals, which allowed conventional FL detection with labeling of target biomarkers. The controller module consisted of two independent units: one calculated FL signals and the other processed imaging biomarkers in multi-view

images. Maximum frequencies of calculations were 10,000 frequencies per second (fps) for controller 1, which calculated FL intensities, and 200 fps for controller 2, which processed imaging biomarkers for the current system. According to the adjustment of suitable thresholds for these parameters, feedback signals could be sent to the sorting module. The sorting module was composed of a direct current (DC) source and electrodes connected with a microchip, and could apply DC voltages to cells flowing in a microchannel of the chip to purify target cells under feedback signals, if necessary. Figure 1 (b) shows the principle of the multi-view module [27,28] used in this study. Firstly, optical paths between BF (red) and FL (blue) lights were separated using dichroic mirror A, as indicated in the figure. Next, angles of mirrors A and B were adjusted; then, BF and FL images were projected onto each half of a CCD component in the camera. An overview of the total system is shown in Fig. 1 (c). The system has a desktop size of 60 cm \times 60 cm.

Figure 2 shows the microchip designed to be suitable for this study. The chip body was fabricated with poly(dimethylsiloxane) (PDMS) attached to a cover glass to apply optical transparency in the observation. Microchannels were placed between the PDMS and the bottom cover glass in the chip with a 2 mm ϕ buffer entrance penetrating the PDMS. The upper stream of the

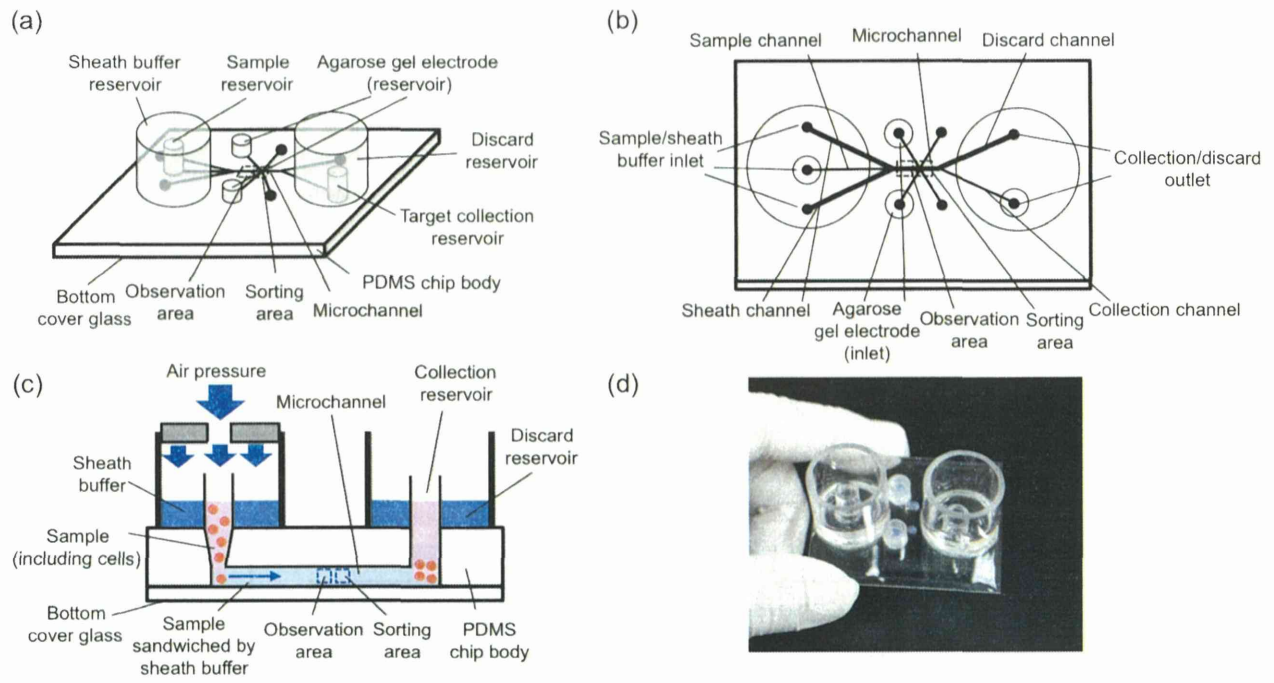


Figure 2. Overview of the microchip. (a) Diagonal, (b) top, and (c) side views of the microchip used in this study. (d) A photograph of the chip. Total chip size is 50 mm × 40 mm. doi:10.1371/journal.pone.0104372.g002

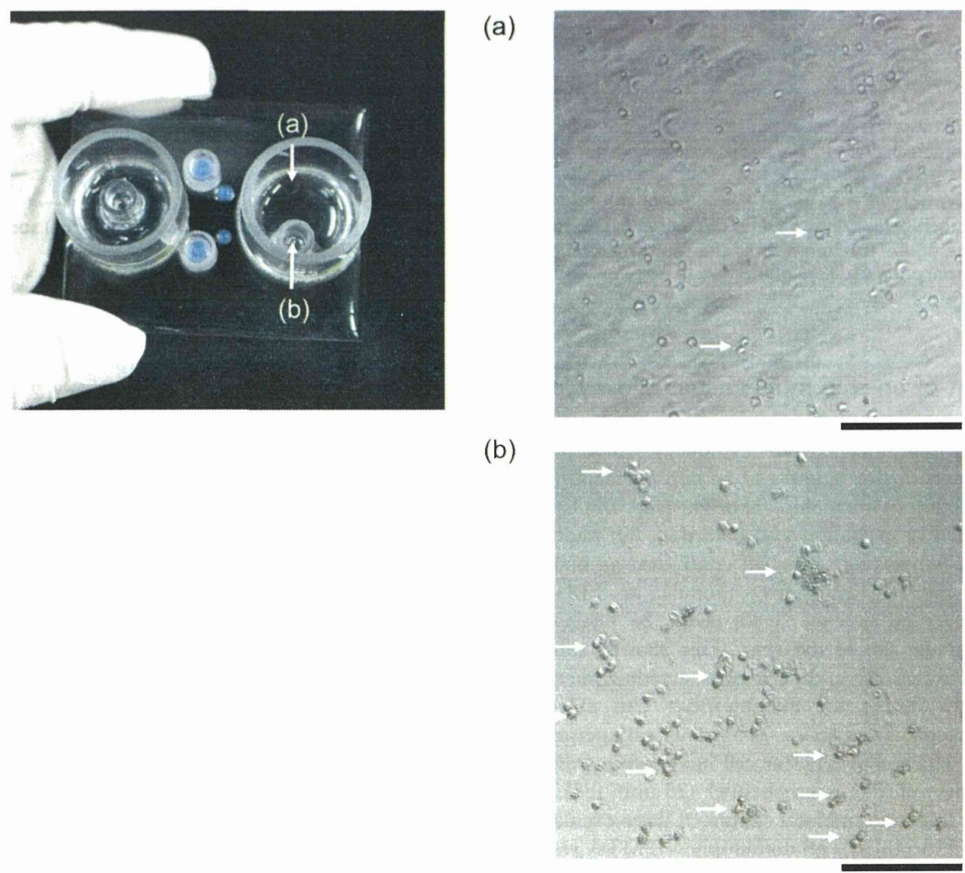


Figure 3. An example of cell sorting. Two photographs of the discarded reservoir (a) and the collection reservoir (b) indicated in the chip photograph are shown. Clustered cells are indicated by white arrows. Bars, 100 μ m. doi:10.1371/journal.pone.0104372.g003

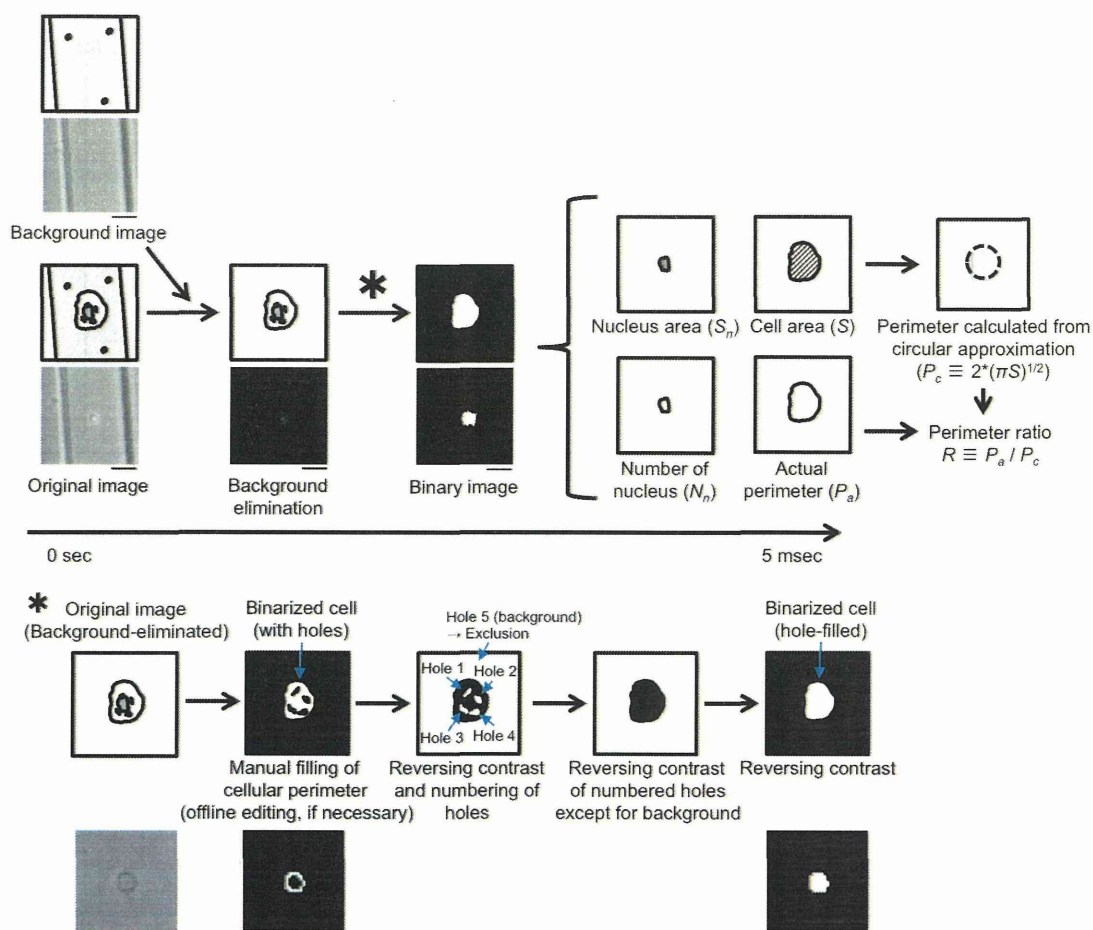


Figure 4. Summary of image processing. Firstly, photographs of both a cell and the background were taken. Next, the background image was subtracted from the cell image and holes were filled. Finally, imaging biomarkers, S , S_n , N_n , and R , were calculated. Bars, 10 μm . The hole-filling procedure is explained as indicated by an asterisk. Bar, 10 μm . doi:10.1371/journal.pone.0104372.g004

microchannel was branched into three channels: the center connected with the sample inlet and the others were a sheath buffer inlet. Both sample and sheath buffers were introduced into the channel with application of air pressure onto both sample and sheath buffer inlets, simultaneously (Fig. 2 (c)). After the meeting of sample and sheath flows, the width of the sample flow was focused in the central one-third, which allowed imaging of each single cell upon the arrangement of all the cells in a straight line.

Images of the linearly arranged cells were obtained through the multi-view module and processed by the system (see Fig. 1), and when a target cell was found, DC voltage (typically 40 V with 100 μsec length) was applied to the cell through the agarose gel electrode (Fig. 2 (a) and (b)) to change its course in the collection channel [11,13]. Figure 3 shows a typical example of the cell sorting with a blood sample of a cancer-implanted rat. As shown in this figure, target cells were set into cell clusters having a large BF area, and once the value of the BF area of the observed cell exceeded the pre-adjusted threshold value, 300 μm^2 in this model case, a sorting voltage was applied to the cell and, finally, target cells were collected into the target collection reservoir. Figures 3 (a) and (b) show pictures taken for discarding (a) and collection (b) reservoirs, respectively. As shown in Fig. 3 (b), large cell clusters (indicated by arrows in the figures) were collected into the collection reservoir. On the other hand, single cells or small cell clusters were collected into the discarding reservoir (Fig. 3 (a)),

indicating the success of target collection using one imaging biomarker, BF area, as a collection parameter. The sorting capacity, which has been determined as the ratio between the number of target cells automatically detected by the system and the actual number of cells in the collection reservoir, was 24%. The low capacity of target cell collection was caused by the higher threshold setting in both recognition and collection processes to prevent 'false positive' sample collection. When the commercially available microbeads were used as a model target in this system, sorting capacity increased to 91%.

As shown in Fig. 3, target cells can be recognized by comparison of the imaging biomarkers with the threshold values pre-adjusted in the system. Figure 4 shows the detail of image processing in the system to obtain imaging biomarkers. Firstly, a background image, which was taken before the assay of flow cytometry, was subtracted from the obtained image with reductions of 8-bit grayscale values in each pixel. Next, the subtracted image was transformed to a binary image using a suitable threshold and pixel errors in the cell, which appeared by almost the same contrast in the cell as in the background, were filled (Fig. 4, asterisk); then, an extracted cell image was obtained. Finally, imaging biomarkers were calculated from the extracted cell image. In the current system, cell area (S) and actual perimeter (P_a) were obtained from the BF image, and nucleus area (S_n) and number of nuclei (N_n) were obtained from the FL image.

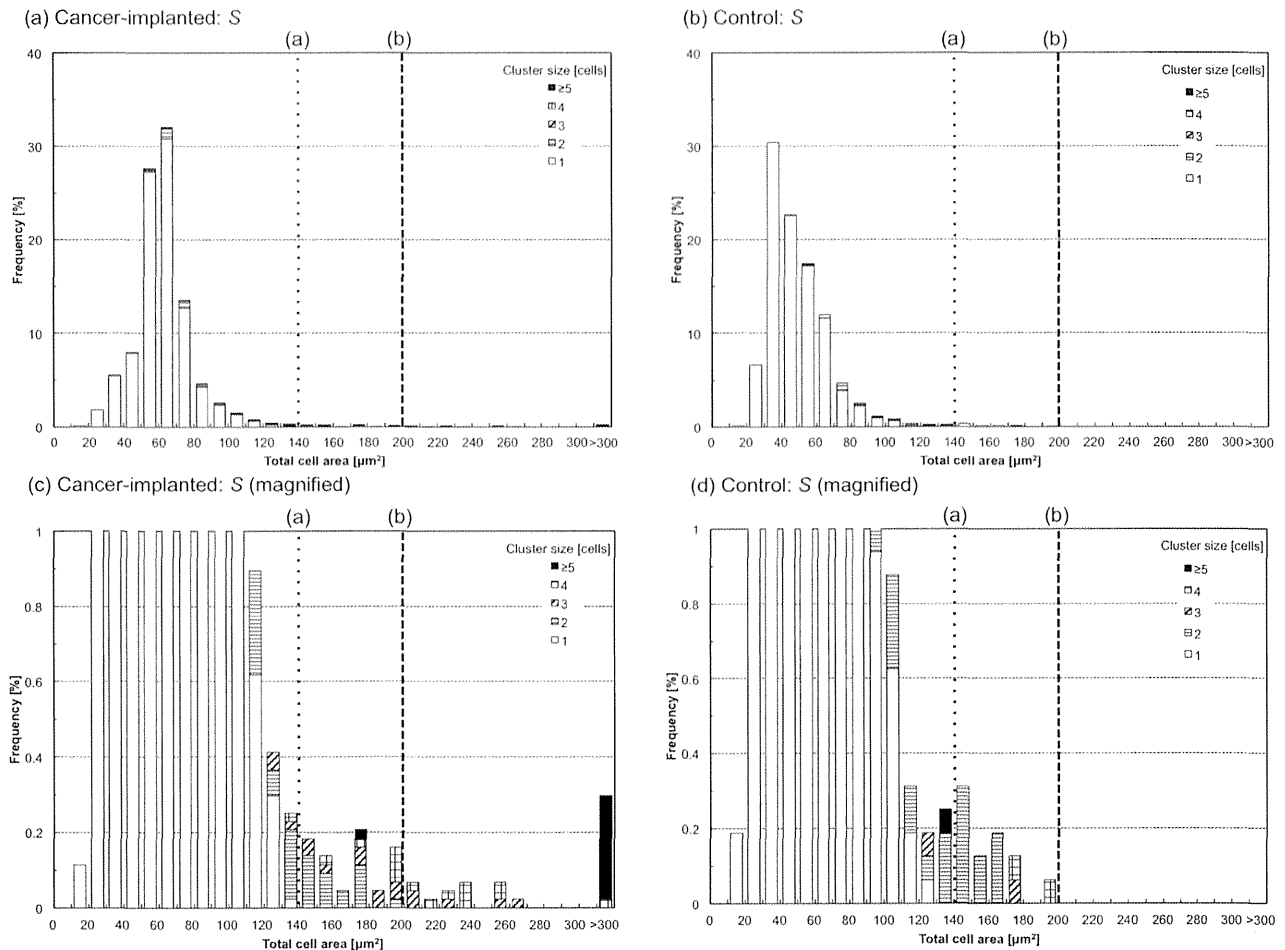


Figure 5. Histograms of total cell area, S , for cancer cell-implanted (a and c) and control blood (b and d). Two threshold values (a) and (b) for cluster identifications are indicated as dotted and dashed lines. doi:10.1371/journal.pone.0104372.g005

Additionally, the perimeter ratio, R , which was obtained as the ratio between P_a and the perimeter calculated from S (P_s) [29], was also obtained. These calculations were performed in real time at 200 fps using controller 2 in Fig. 1, and in this study, manual calculations of the imaging biomarkers, including a few modifications for apparently failed auto-calculations caused by the failure of continuous detection of the cell perimeter in the hole filling procedure, were also performed as post-processing to confirm the reliabilities of the obtained imaging biomarker values.

Detection of clustered cells in cancer-implanted rat blood using imaging biomarkers

After the success of the system development, its performance for the identification of specific target cells using imaging biomarkers was quantitatively evaluated. Blood of a rat in which a rat prostate cancer cell line (MAT-LyLu) had been implanted was chosen as a model sample, and clustered cells in the blood were set as a target for the detection using imaging biomarkers with the developed system. One approach anticipated to achieve successful detection of the clusters is the use of cell area; therefore, areas in BF images (i.e., total cell area, S) and FL images (i.e., total nucleus area, S_n) were measured using the system. Figures 5 and 6 are histograms of S (Fig. 5) and S_n (Fig. 6) for cells in the cancer-implanted blood ($N = 4375$), shown with healthy rat blood as its control ($N = 1599$).

Detailed numbers including S and S_n are also summarized in Table 1. From the results, clustered cells were observed at a count of 237 in cancer-implanted samples (5.4% of the total) and a count of 56 in the control (3.5% of the total). In addition, two clear threshold values were found in both S and S_n ; that is, (a) all cells having S larger than 140 μm^2 (count of 61, 1.4% of the total, for cancer-implanted samples and 13, 0.8% of the total, for the control) and S_n larger than 80 μm^2 (count of 34, 0.8% of the total, for cancer-implanted samples and 1, 0.1% of the total, for the control) were clustered cells, as indicated by the dotted lines in Figs. 5 and 6, and (b) the clustered cells having S larger than 200 μm^2 (count of 27, 0.6% of the total) and S_n larger than 90 μm^2 (count of 26, 0.6% of the total) were specifically observed in cancer cell-implanted blood. These results indicate that some cell clusters can be identified by using S and S_n (61 of 237, 26% of all clusters, for S and 34 of 237, 14% of all clusters, for S_n) as parameters for detection.

Obtained pictures were manually analyzed one by one with measured values of S and S_n . Figure 7 shows examples of single- and double-cell images having one, two, or three nuclei obtained from cancer-implanted and control blood, respectively. As shown in Fig. 7, the following 3 results were obtained: (i) single cells having multiple nuclei numbering more than two were specifically included in the cancer cell-implanted blood (count of 133, 3.2% of total single cells in cancer-implanted samples), (ii) two-cell clusters

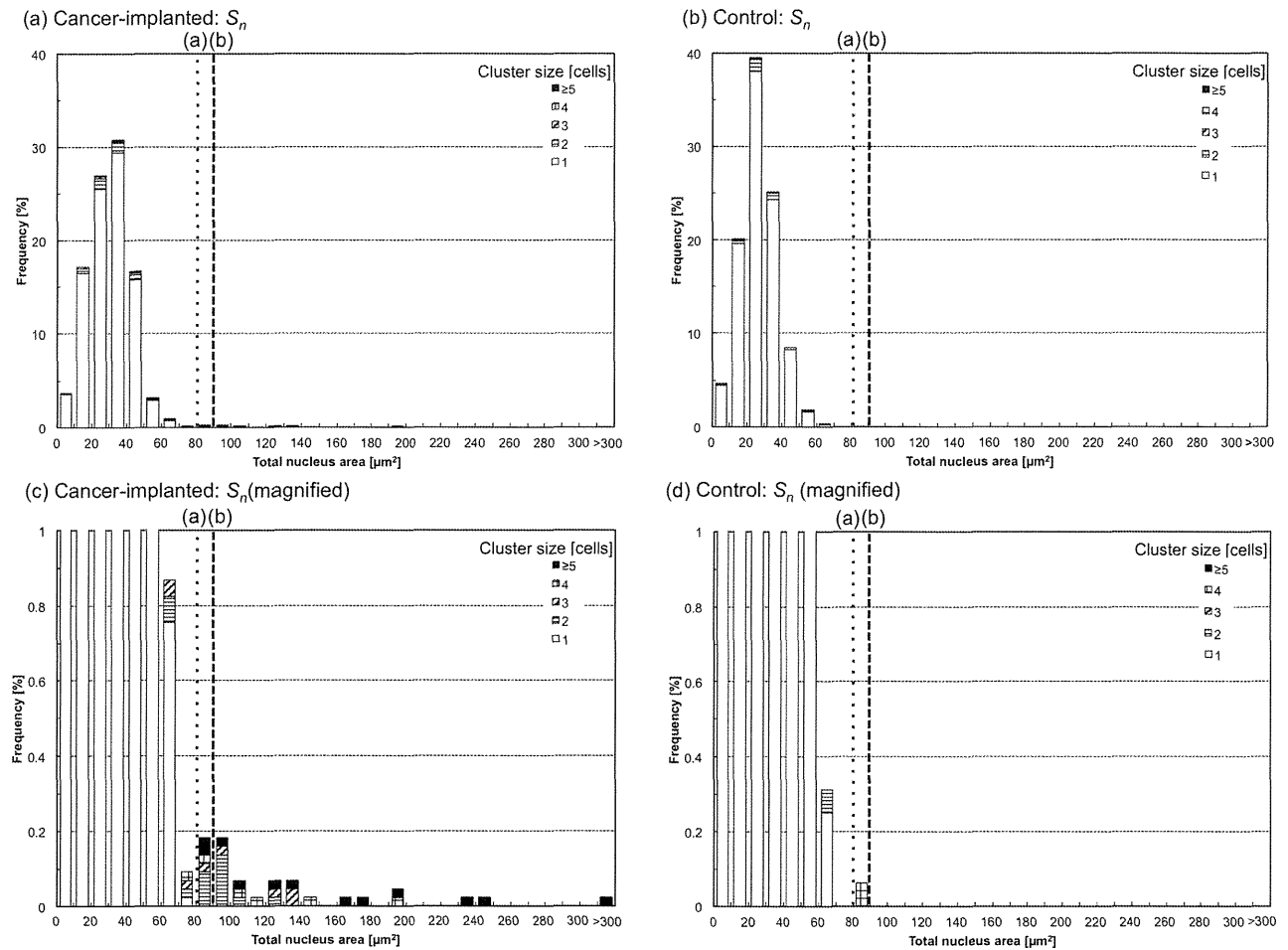


Figure 6. Histograms of total nucleus area, S_n , for cancer cell-implanted (a and c) and control blood (b and d). Two threshold values (a) and (b) for cluster identifications are indicated as dotted and dashed lines. doi:10.1371/journal.pone.0104372.g006

having only one nucleus seemed to be single cells to which a small particle (possibly debris of a hemolyzed red cell) was attached (count of 126, 72% of total two-cell clusters in cancer-implanted samples and count of 41, 84% of total two-cell clusters in control), and (iii) two-cell clusters having two nuclei were either true clusters or two independent cells flowing alongside each other (count of 48, including 2 clusters having 3 nuclei caused by the inclusion of a cell with multiple nuclei, 28% of total two-cell clusters in cancer-implanted samples and count of 8, 16% of total two-cell clusters in control). The first of these results shows the potential for the detection of implanted cancer cells having multiple nuclei, and the second can be thought of as single cells in general. The third in principle makes it difficult to distinguish two-cell clusters from two single cells using pictures; therefore, such two-cell “clusters” were also contained in control blood.

Figure 8 shows typical clustered cells composed of more than 3 cells. As shown in the figure and also in Table 1, a few clusters composed of more than 3 cells were also detected in control blood (count of 7 in total), with the maximum cell number of 6. However, they seemed to be single or two independent cells to which small particles were attached (i.e., the same as result (ii) in Fig. 7), which could also be confirmed by the number of nuclei, N_n , in the cluster, which had a maximum of 2. On the other hand, clusters contained in cancer-implanted blood were composed of more than 3 cells, with 15 cells at maximum, which was also

confirmed by N_n in the cluster being more than 3. It is unlikely for more than 3 cells to be flowing alongside each other; therefore, we concluded that clusters composed of more than 3 cells containing more than 3 nuclei were truly clustered cells in the blood. Such large clusters were contained in cancer cell-implanted blood at a count of 33 (7 counts, 21% of 3-cell clusters, 12 counts, 75% of 4-cell clusters, 14 counts, 100% of ≥ 5 -cell clusters, and 0.8% of the total). Measured values of N_n are summarized in Fig. 9 (a) (and also in Table 1). As shown in this figure, more than 99% of images in control blood had a single nucleus, and cell clusters having more than 3 nuclei were not contained in the blood. Figure 9 (b) also shows N_n summarized from the perspective of cluster size. As shown in the figure, large clusters in cancer-implanted blood had many nuclei, typically more than 3, indicating the possibility of the cluster formation of CTCs in the blood.

As shown in the above results, N_n is one useful imaging biomarker to identify cell clusters in blood; however, only using this marker for identification is insufficient because single cells having multiple nuclei were also contained in cancer cell-implanted blood, as shown in Fig. 7; therefore, we evaluated another imaging biomarker, perimeter ratio (R), for the identification of clustered cells. R is defined as the ratio between the actual perimeter obtained from the cell image and the perimeter calculated with a circle approximation of S . A low value of R indicates distorted conformation of the cell away from a circular

Table 1. Summary of total cell area, S , total nucleus area, S_n , number of nuclei, N_n , and perimeter ratio, R , for each cluster size.

Cancer-implemented (N = 4375)			Total cell area, S [μm^2]					Total nucleus area, S_n [μm^2]				
Cluster [cells]	Frequency [counts]	Frequency [%]	Average	Median	S.D.	Max.	Min.	Average	Median	S.D.	Max	Min
1	4138	94.58	62	62	15	133	11	30	31	12	73	7
2	174	3.98	88	75	33	194	36	36	33	19	122	10
3	33	0.75	133	124	58	263	53	45	33	35	134	12
4	16	0.37	219	208	57	393	136	74	52	46	195	24
≥ 5	14	0.32	515	421	180	1163	179	149	131	85	342	37
≥ 2	237	5.4	129	81	130	1163	36	47	35	41	342	10
Cancer-implemented (continued)			Number of nuclei, N_n					Perimeter ratio, R				
Cluster [cells]	Frequency [counts]	Frequency [%]	Average	Median	S.D.	Max.	Min.	Average	Median	S.D.	Max	Min
1	4138	94.58	1.03	1.00	0.20	3	1	0.96	0.96	0.02	1.00	0.90
2	174	3.98	1.30	1.00	0.50	3	1	0.89	0.91	0.05	0.97	0.76
3	33	0.75	1.82	2.00	0.88	4	1	0.83	0.82	0.06	0.95	0.67
4	16	0.37	2.75	3.00	1.13	4	1	0.84	0.84	0.07	0.95	0.74
≥ 5	14	0.32	5.00	5.00	1.15	10	2	0.80	0.80	0.03	0.89	0.79
≥ 2	237	5.4	1.70	1.00	1.26	10	1	0.87	0.89	0.06	0.97	0.67
Control (N = 1599)			Total cell area, S [μm^2]					Total nucleus area, S_n [μm^2]				
Cluster [cells]	Frequency [counts]	Frequency [%]	Average	Median	S.D.	Max.	Min.	Average	Median	S.D.	Max	Min
1	1543	96.50	48	44	16	121	11	27	26	10	69	7
2	49	3.06	99	83	36	169	40	28	28	12	61	7
3	3	0.19	119	127	62	177	54	23	24	10	32	13
4	2	0.13	187	187	14	197	177	51	51	43	81	20
≥ 5	2	0.13	116	116	24	133	99	32	44	18	57	32
≥ 2	56	3.5	104	88	39	197	40	29	28	14	81	7
Control (continued)			Number of nuclei, N_n					Perimeter ratio, R				
Cluster [cells]	Frequency [counts]	Frequency [%]	Average	Median	S.D.	Max.	Min.	Average	Median	S.D.	Max	Min
1	1543	96.50	1.00	1.00	0.00	1	1	0.96	0.96	0.02	1.00	0.90
2	49	3.06	1.16	1.00	0.37	2	1	0.82	0.84	0.05	0.91	0.70
3	3	0.19	1.67	2.00	0.58	2	1	0.83	0.83	0.06	0.89	0.77
4	2	0.13	1.50	1.50	0.71	2	1	0.81	0.81	0.08	0.86	0.75
≥ 5	2	0.13	1.00	1.00	0.00	1	1	0.81	0.81	0.01	0.82	0.80
≥ 2	56	3.5	1.20	1.00	0.40	2	1	0.82	0.83	0.05	0.91	0.70

doi:10.1371/journal.pone.0104372.t001

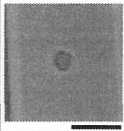

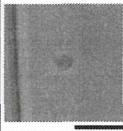

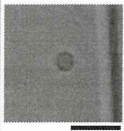
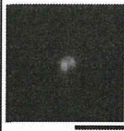




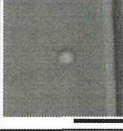

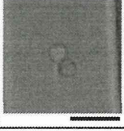

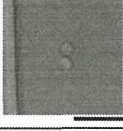

Cancer-implanted					Control				
Cluster size (N_n)	BF	FL	S [μm^2]	S_n [μm^2]	Cluster size (N_n)	BF	FL	S [μm^2]	S_n [μm^2]
1 (1) $n = 4005$			59	35	1 (1) $n = 1543$			55	21
1 (2) $n = 123$			57	41	1 (2)	N.A.			
1 (3) $n = 10$			72	47	1 (3)	N.A.			
2 (1) $n = 126$			67	26	2 (1) $n = 41$			69	40
2 (2) $n = 48$			117	74	2 (2) $n = 8$			73	61

Figure 7. Typical cell images for single and double cells in cancer cell-implanted and control blood. Each data count (n) indicates the image number having the same cluster size and N_n . Bars, 20 μm .
doi:10.1371/journal.pone.0104372.g007

shape, which was expected for cell clusters. Figure 10 shows the relationship between the average value of R and cell cluster size for a cancer-implanted sample (detailed numbers are also shown in Table 1). As shown in the figure and table, all single cells had R higher than 0.90, with an average of 0.96, indicating that all cells having R smaller than 0.90 were clusters composed of more than 2 cells. On the other hand, R values for clusters composed of more than 2 cells were lower than 0.90 on average, and in detail, 131 clusters in cancer-implanted samples (55% of all clusters) and 55 clusters in control (98% of all clusters) had R lower than 0.90. Moreover, all large clusters composed of more than 3 cells having more than 3 nuclei, specifically observed only in cancer-implanted blood, had R lower than 0.90. These results indicate that more than half of the clusters, especially large clusters, could be identified by using R as an imaging biomarker.

According to the above results, large cluster formation of cancer cells in the blood was strongly expected. To confirm this, clusters larger than 300 μm^2 were collected by performing cell sorting in the chip, and their cell types were identified by measuring genome errors in the cells. Firstly, target genes that were included in the MAT-LyLu chromosome with abnormal copy numbers were searched by comparative genomic hybridization (CGH) assay using the cell line, with liver tissue of the rat as a reference. Two particularly abundant genes, *csrp2* and *zdhhc17* located on chromosome 7q13, were found (Fig. 11 (a)) and set as target genes for the identification of cancer cells in the blood. Next, the TaqMan copy number assay was performed for cells collected in

both the collection reservoir and the discarded reservoir (see Fig. 3). From the results, increases of copy numbers for both *csrp2* and *zdhhc17* were specifically observed for clustered cells collected in the collection reservoir (Fig. 11 (b)). These results indicate that large clusters, which were specifically observed in cancer cell-implanted blood, were CTCs.

Discussion

In this study, four imaging biomarkers, cell area, nucleus area, number of nuclei, and perimeter ratio (S , S_n , N_n , and R), were evaluated for the identification of cell clusters in the blood. From the results, some threshold values were obtained for each imaging biomarker, namely, (1) S larger than 200 μm^2 and (2) S_n larger than 90 μm^2 were specific to cancer cell-implanted blood. In addition, (3) N_n higher than 3 was also specific to cancer cell-implanted blood. Finally, (4) all clustered cells composed of more than 3 cells having N_n higher than 3, which was specific to cancer cell-implanted blood, had R lower than 0.90. According to these results, the use of R is one useful approach for the identification of clustered cells having multiple nuclei numbering more than 3, which are specific to cancer cell-implanted blood. S and S_n are also useful parameters for the identification of extremely large clusters, which are quite likely to be CTCs. For small clusters composed of two cells, it is in principle difficult to distinguish whether the cluster is an actual cluster or two independent cells flowing alongside each other by using image-based analysis. One potential approach to distinguish these possibilities is the

Cancer-implanted					Control				
Cluster size (N_n)	BF	FL	S [μm^2]	S_n [μm^2]	Cluster size (N_n)	BF	FL	S [μm^2]	S_n [μm^2]
3 (3) $n = 6$			251	126	3 (1) $n = 1$			53	12
4 (4) $n = 4$			258	147	4 (1) $n = 1$			197	20
6 (6) $n = 1$			388	179	5 (1) $n = 1$			99	32
15 (max., 10) $n = 1$			1163	342	6 (max., 1) $n = 1$			133	50

Figure 8. Typical cell images for clustered cells composed of more than three cells in cancer cell-implanted and control blood. Each data count (n) indicates the image number having the same cluster size and N_n . Bars, 20 μm . doi:10.1371/journal.pone.0104372.g008

combination of the image-based analysis suggested in this study with a molecular analytical approach, such as quantitative gene copy number assays of the targeted cells. The system developed in this study has been combined with a cell sorting unit and can perform the combination measurement of multi-imaging analysis with molecular analysis, as shown in Fig. 11, which indicates the advantage of our developed system.

For the detection of CTCs, some methods were suggested. The principles were in general separated into two kinds; one was based on the chemical reaction and the other was physical detection. The former is in general based on the labeling of target molecules on the CTCs with antibodies, and it was sometimes combined with microfabrication technologies to improve detection sensitivities [6,7]. However, this approach sometimes yielded false-negative detection because of the variety of molecular expression levels in

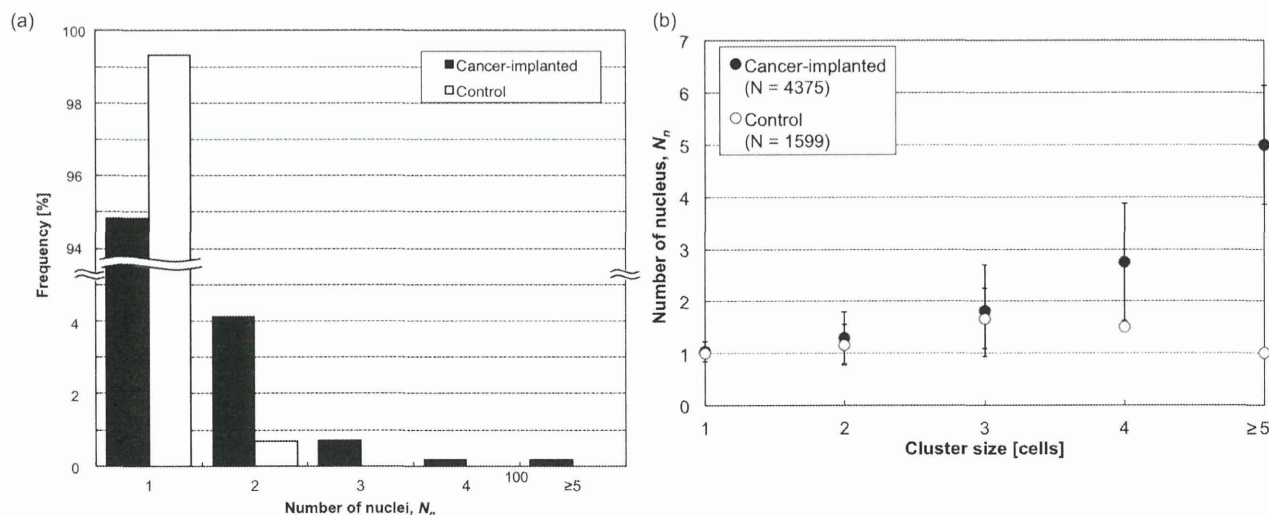


Figure 9. Summary of the number of nuclei, N_n . (a) A histogram of N_n obtained from cancer cell-implanted and control blood. (b) The relationship between N_n and cell cluster size. doi:10.1371/journal.pone.0104372.g009

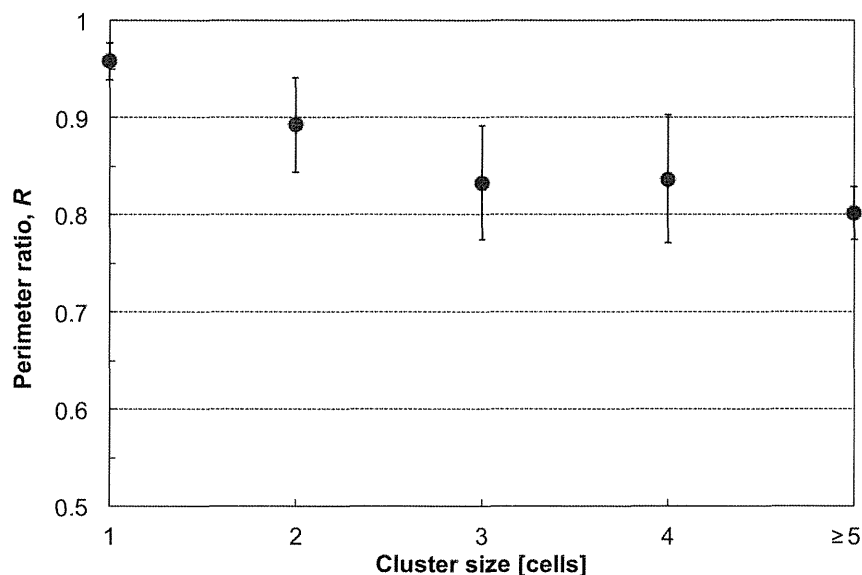


Figure 10. The relationship between perimeter ratio, R, and cell cluster size obtained from cancer cell-implanted blood.
doi:10.1371/journal.pone.0104372.g010

CTCs. For this latter case, various physical parameters of CTCs such as cell diameter [4,16,17] and dielectrophoretic properties [5] have been used with a combination of microfabrication technologies. According to the results in this study, cell size (*S*) is one useful parameter to find irregular cells in blood samples such as

clustered cells; however, the use of only one parameter is insufficient for the exhaustive detection of CTCs. Our developed system can use various parameters including both chemical and physical properties to find target cells, which would also be useful for the detection of various CTCs.

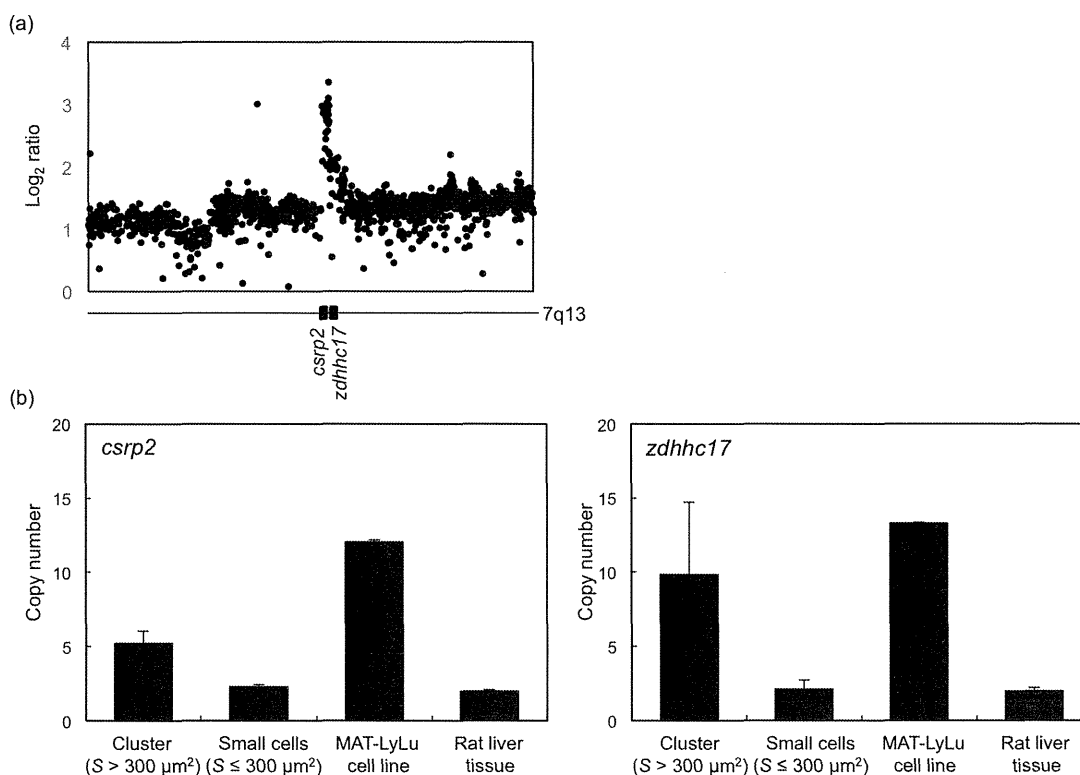


Figure 11. Results of quantitative gene copy number assays. (a) Results of CGH assays performed for the MAT-LyLu cell line. Liver tissue of the rat was used as a reference. Gene amplifications for *csrp2* and *zdhhc17* located on chromosome 7q13 were found. (b) Results of TaqMan copy number assays performed with clusters larger than 300 μm² collected in the collection reservoir, and cells smaller than 300 μm² collected in the discarded reservoir. Results of the assays for the MAT-LyLu cell line (positive control) and liver tissue (negative control) are also shown.
doi:10.1371/journal.pone.0104372.g011

In this study, large clusters were specifically observed in cancer cell-implanted blood, and an approach for finding these clusters in the blood has possibility for the development of a new cancer metastasis diagnostic method. Results in this study were obtained using hemolyzed blood samples *in vitro*; therefore, the large cluster formations should also be confirmed for blood *in vivo* as a next step to achieve such a new diagnostic method. One possibility for the mechanism of large cluster formation is an aggregation of implanted cancer cells by immune reaction of the rat with antibody formation. In this study, blood samples were picked up from the rat 2 weeks after implantation; therefore, time-course measurements of cluster formations after implantation might be one useful way to confirm the above possibility, and our developed system can also be used to confirm this.

Conclusion

In this study, an on-chip multi-imaging flow cytometry system was developed to find cell clusters in blood samples. The system can take both BF and FL pictures simultaneously, and can obtain imaging biomarkers; cell area, nucleus area, number of nuclei, and perimeter ratio (S , S_n , N_n , and R), in real time. By using the developed system, sample blood of rats in which cancer cells had been pre-implanted was measured and compared with that of

healthy rats. In terms of the results, clustered cells having (1) S larger than $200 \mu\text{m}^2$ and (2) S_n larger than $90 \mu\text{m}^2$ were specifically observed in cancer cell-implanted blood, but were not observed in healthy rats. In addition, (3) N_n higher than 3 was specific for cancer-implanted blood and (4) R smaller than 0.90 was specific for all clusters having N_n higher than 3, which were specific for cancer-implanted blood. Finally, quantitative gene copy number assay was performed for the large clusters, and they were shown to be CTCs. These results indicate the usefulness of the imaging biomarkers for characterizing clusters, and that the developed system is useful to identify clustered CTCs in blood.

Acknowledgments

We gratefully thank Mr. S. Kawada and Ms. H. Mikami for technical assistance.

Author Contributions

Conceived and designed the experiments: HK TA KN YM KY. Performed the experiments: HK HT YN KS AH MO MG TA. Analyzed the data: HK KS AH MO MG TA KN YM KY. Contributed reagents/materials/analysis tools: HK HT YN KS AH MO MG TA KN YM KY. Wrote the paper: HK KY.

References

- Cristofanilli M, Budd GT, Ellis MJ, Stopeck A, Matera J, et al. (2004) Circulating tumor cells, disease progression, and survival in metastatic breast cancer. *N Engl J Med* 351: 781–791.
- Sethi N, Kang Y (2011) Unravelling the complexity of metastasis - molecular understanding and targeted therapies. *Nat Rev Cancer* 11: 735–748.
- Yu M, Stott S, Toner M, Maheswaran S, Haber DA (2011) Circulating tumor cells: approaches to isolation and characterization. *J Cell Biol* 192: 373–382.
- Davis JA, Inglis DW, Morton KJ, Lawrence DA, Huang LR, et al. (2006) Deterministic hydrodynamics: taking blood apart. *Proc Natl Acad Sci U S A* 103: 14779–14784.
- Gascoyne PR, Noshari J, Anderson TJ, Becker FF (2009) Isolation of rare cells from cell mixtures by dielectrophoresis. *Electrophoresis* 30: 1388–1398.
- Nagrath S, Sequist LV, Maheswaran S, Bell DW, Irimia D, et al. (2007) Isolation of rare circulating tumour cells in cancer patients by microchip technology. *Nature* 450: 1235–1239.
- Stott SI, Hsu CH, Tsukrov DI, Yu M, Miyamoto DT, et al. (2010) Isolation of circulating tumor cells using a microvortex-generating herringbone-chip. *Proc Natl Acad Sci U S A* 107: 18392–18397.
- Zheng S, Lin HK, Lu B, Williams A, Datar R, et al. (2011) 3D microfilter device for viable circulating tumor cell (CTC) enrichment from blood. *Biomed Microdevices* 13: 203–213.
- Budd GT, Cristofanilli M, Ellis MJ, Stopeck A, Borden E, et al. (2006) Circulating tumor cells versus imaging—predicting overall survival in metastatic breast cancer. *Clin Cancer Res* 12: 6403–6409.
- Danila DC, Heller G, Gignac GA, Gonzalez-Espinoza R, Anand A, et al. (2007) Circulating tumor cell number and prognosis in progressive castration-resistant prostate cancer. *Clin Cancer Res* 13: 7053–7058.
- Takahashi K, Hattori A, Suzuki I, Ichiki T, Yasuda K (2004) Non-destructive on-chip cell sorting system with real-time microscopic image processing. *J Nanobiotechnology* 2: 5.
- Hayashi M, Hattori A, Kim H, Terazono H, Kaneko T, et al. (2011) Fully automated on-chip imaging flow cytometry system with disposable contamination-free plastic re-cultivation chip. *Int J Mol Sci* 12: 3618–3634.
- Yasuda K, Hattori A, Kim H, Terazono H, Hayashi M, et al. (2013) Non-destructive on-chip imaging flow cell-sorting system for on-chip cellomics. *Microfluidics and Nanofluidics* 14: 907–931.
- Vona G, Sabile A, Louha M, Struk V, Romana S, et al. (2000) Isolation by size of epithelial tumor cells - A new method for the immunomorphological and molecular characterization of circulating tumor cells. *American Journal of Pathology* 156: 57–63.
- Desitter I, Guerrouahen BS, Benali-Furet N, Wechsler J, Janne PA, et al. (2011) A New Device for Rapid Isolation by Size and Characterization of Rare Circulating Tumor Cells. *Anticancer Research* 31: 427–441.
- Hosokawa M, Kenmotsu H, Koh Y, Yoshino T, Yoshikawa T, et al. (2013) Size-Based Isolation of Circulating Tumor Cells in Lung Cancer Patients Using a Microcavity Array System. *Plos Onc* 8.
- Hosokawa M, Yoshikawa T, Negishi R, Yoshino T, Koh Y, et al. (2013) Microcavity Array System for Size-Based Enrichment of Circulating Tumor Cells from the Blood of Patients with Small-Cell Lung Cancer. *Analytical Chemistry* 85: 5692–5698.
- Abdalla F, Boder J, Markus R, Hashmi H, Buhmeida A, et al. (2009) Correlation of nuclear morphometry of breast cancer in histological sections with clinicopathological features and prognosis. *Anticancer Res* 29: 1771–1776.
- Buhmeida A, Algars A, Ristamaki R, Collan Y, Syrjanen K, et al. (2006) Nuclear size as prognostic determinant in stage II and stage III colorectal adenocarcinoma. *Anticancer Res* 26: 455–462.
- de Andrea CE, Pettrilli AS, Jesus-Garcia R, Bleggi-Torres LF, Alves MT (2011) Large and round tumor nuclei in osteosarcoma: good clinical outcome. *Int J Clin Exp Pathol* 4: 169–174.
- Deans GT, Hamilton PW, Watt PC, Heatley M, Williamson K, et al. (1993) Morphometric analysis of colorectal cancer. *Dis Colon Rectum* 36: 450–456.
- Dundas SA, Laing RW, O’Cathain A, Scddon I, Slater DN, et al. (1988) Feasibility of new prognostic classification for rectal cancer. *J Clin Pathol* 41: 1273–1276.
- Meachem MD, Burgess HJ, Davies JL, Kidney BA (2012) Utility of nuclear morphometry in the cytologic evaluation of canine cutaneous soft tissue sarcomas. *J Vet Diagn Invest* 24: 525–530.
- Sokmen S, Sarioglu S, Fuzun M, Terzi C, Kupelioglu A, et al. (2001) Prognostic significance of angiogenesis in rectal cancer: a morphometric investigation. *Anticancer Res* 21: 4341–4348.
- Tennant TR, Kim H, Sokoloff M, Rinker-Schaeffer CW (2000) The Dunning model. *Prostate* 43: 295–302.
- Hattori A, Yasuda K (2010) Comprehensive Study of Microgel Electrode for On-Chip Electrophoretic Cell Sorting. *Japanese Journal of Applied Physics* 49: 06GM04.
- Hattori A, Kim H, Terazono H, Odaka M, M G, et al. (2014) Identification of cells using morphological information of bright field/fluorescent multi-imaging flow cytometer images. *Japanese Journal of Applied Physics*, in press.
- Kinosita K, Jr., Itoh H, Ishiwata S, Hirano K, Nishizaka T, et al. (1991) Dual-view microscopy with a single camera: real-time imaging of molecular orientations and calcium. *J Cell Biol* 115: 67–73.
- Nomura F, Kaneko T, Hattori A, Yasuda K (2011) Label-Free Shape-Based Selection of Cardiomyocytes with on-Chip Imaging Cell Sorting System. *J Bioprocess Biotechniq* S3:003.